

Thermal conductivity of monolayer MoS₂, MoSe₂, and WS₂: Interplay of mass effect, interatomic bonding and anharmonicity

Bo Peng¹, Hao Zhang^{1,*}, Hezhu Shao², Yuchen Xu¹, Xiangchao Zhang¹ and Heyuan Zhu¹

¹*Shanghai Ultra-precision Optical Manufacturing Engineering Center,*

Department of Optical Science and Engineering,

Fudan University, Shanghai 200433, China

²*Ningbo Institute of Materials Technology and Engineering,*

Chinese Academy of Sciences, Ningbo 315201, China

Phonons are essential for understanding the thermal properties in monolayer transition metal dichalcogenides, which limit their thermal performance for potential applications. We investigate the lattice dynamics and thermodynamic properties of MoS₂, MoSe₂, and WS₂ by first principles calculations. The obtained phonon frequencies and thermal conductivities agree well with the measurements. Our results show that the thermal conductivity of MoS₂ is highest among the three materials due to its much lower average atomic mass. We also discuss the competition between mass effect, interatomic bonding and anharmonic vibrations in determining the thermal conductivity of WS₂. Strong covalent W-S bonding and low anharmonicity in WS₂ are found to be crucial in understanding its much higher thermal conductivity compared to MoSe₂.

I. INTRODUCTION

Monolayer transition metal dichalcogenides, MX₂ (M = Mo, W; X = S, Se), have aroused much interest recently due to their remarkable properties for applications in next-generation nanoelectronic and energy conversion devices¹⁻³. Since all these applications are closely related to its thermal properties, it is necessary to investigate the lattice dynamics and thermodynamic properties of MX₂. For instance, high-performance electronic devices strongly depend on high thermal conductivity for highly efficient heat dissipation, while low thermal conductivity is preferred in thermoelectric application.

In semiconductors, heat is carried by the atomic vibrations that are quantized as

phonons⁴. Theoretical predictions based on the phonon Boltzmann transport equation have found that monolayer WS₂ has the highest thermal conductivity (142 W/mK) at room temperature, then followed by MoS₂ (103 W/mK) and MoSe₂ (54 W/mK)⁵. However, the measured thermal conductivity for monolayer MoS₂ and WS₂ is 34.5 ± 4 W/mK⁶ and 32 W/mK⁷, respectively, which is much lower than the theoretical predictions. Furthermore, various phonon properties such as interatomic bonding and anharmonic vibrations still lack a unified understanding. The parameters that affect phonon transport include crystal structure, atomic mass, interatomic bonding, and anharmonicity⁸⁻¹⁰. Generally there are four rules for finding a nonmetallic crystal with higher thermal conductivity, including (i) lower average atomic mass, (ii) stronger interatomic bonding, (iii) simpler crystal structure, and (iv) lower anharmonicity⁸. All monolayer MX₂ compounds have similar crystal structures, while conditions (i) and (ii) imply a larger Debye temperature, and condition (iv) means smaller Grüneisen parameter. Recent theoretical investigation has provided a quantitative analysis of the roles of mass, structure, and bond strength in thermal expansion and thermomechanics of MX₂¹¹. However, the roles of mass, interatomic bonding, and anharmonic vibrations in phonon transport still remain uninvestigated. Clear knowledge of the underlying physics will be helpful for understanding and modulating the thermal transport in MX₂, for example, through doping other M or X atoms^{12,13}.

Here we investigate fundamental vibrational properties to understand thermal transport in MoS₂, MoSe₂, and WS₂. The measured phonon frequencies are well reproduced in our calculations. The thermodynamic properties are calculated within quasi-harmonic approximation, and the calculated thermal conductivities agree well with the measurements. Combining first principles calculations and the Slack model, the roles of mass, interatomic bonding, and anharmonicity in thermal transport are clearly revealed.

II. METHODOLOGY

All calculations are implemented in the Vienna *ab initio* simulation package (VASP) based on the density functional theory (DFT) method¹⁴. The Perdew, Burke, and Ernzerhof (PBE) parametrization within the generalized gradient approximation (GGA) is used for the exchange-correlation functional. A plane-wave basis set is employed with the kinetic energy cutoff of 600 eV. A $15 \times 15 \times 1$ **k**-mesh is used during structural relaxation for the unit cell

TABLE I: Calculated lattice parameters and band gap of monolayer MX_2 . Experimental data are also given in parentheses for comparison.

	MoS ₂	MoSe ₂	WS ₂
a (Å)	3.165 (3.160 ^a)	3.300 (3.288 ^a)	3.163 (3.154 ^b)
E_g (eV)	1.81 (1.88 ^c)	1.56 (1.57 ^d)	1.97 (1.95 ^e)

^a Reference¹⁸

^b Reference¹⁹

^b Reference²⁰

^b Reference²¹

^b Reference²²

until the energy differences are converged within 10^{-6} eV, with a Hellman-Feynman force convergence threshold of 10^{-4} eV/Å. We maintain the interlayer vacuum spacing larger than 12 Å to eliminate the interaction with periodic boundary condition.

In the calculation of phonon dispersion, the harmonic interatomic force constants (IFCs) are obtained by density functional perturbation theory (DFPT) using the supercell approach, which calculates the dynamical matrix through the linear response of electron density¹⁵. The $5 \times 5 \times 1$ supercell with $5 \times 5 \times 1$ \mathbf{k} -mesh is used to ensure the convergence. The phonon dispersion is obtained using the Phonopy code with the harmonic IFCs as input¹⁶.

III. RESULTS AND DISCUSSION

A. Crystal structures

Monolayer MX_2 has honeycomb structure with space group $P6m2$ ¹⁷ as shown in fig. 1. An M atom layer is sandwiched between two X atom layers, connected by covalent bonds. The optimized lattice parameters of all studied MX_2 are shown in table I. Our GGA calculations overestimate the lattice parameters by 0.16%, 0.36%, and 0.29%, respectively, which is a general feature of the GGA functional.

The electronic structures of all studied MX_2 are calculated by DFT method. As shown in table I, the calculated band gap is consistent with the measurements²⁰⁻²². The total and atom projected density of states (DOS) are shown in fig. 2. The total DOS from -7 to 10

eV is mainly composed of M- d and X- p states, and the bands on each side of the band gap originate primarily from M- d states, which is in agreement with previous work²³. Due to a less localized DOS of W atoms, the overlap between W- d and S- p state in the valence band of WS₂ from -7 to 0 eV is larger than other two materials, indicating a strong covalent $p-d$ bonding. Similar large overlap between W- d and S- p state in WS₂ from 0 to 12 eV tends to increase the widths of the conduction bands.

Fig. 3 presents the electronic charge density of all studied MX₂ in the $[1\bar{1}0]$ plane. For MoS₂ and MoSe₂, the highest charge density is found to be on the Mo atoms due to the strongly localized DOS of Mo atoms, while for WS₂, S atoms have the highest charge density. As shown in fig. 3, the W-S bonding is the strongest, whereas the Mo-Se bonding is weaker than the Mo-S bonding, which is consistent with the projected DOS in fig. 2. Usually, strong interatomic bonding and low average atomic mass imply a large Debye temperature, leading to a high thermal conductivity. From fig. 2, it is found that the d state of transition metal M play an important role in determining the interatomic bonding, which will further affect the heat transport in these three materials.

B. Phonon spectra

The phonon spectra of all studied MX₂ structures are calculated using the supercell approach, with the real-space force-constants calculated in the density-functional perturbation theory (DFPT)¹⁵ within the Phonopy code¹⁶. Fig. 4 presents the phonon spectra along several high symmetry directions, together with the corresponding projected phonon density of states (PDOS). The primitive cell of monolayer MX₂ contains 3 atoms, corresponding to three acoustic and six optical phonon branches. The average acoustic Debye temperature for monolayer MX₂ is determined from²⁴

$$\frac{1}{\theta_D^3} = \frac{1}{2} \left(\frac{1}{\theta_{LA}^3} + \frac{1}{\theta_{TA}^3} \right), \quad (1)$$

where θ_i for each acoustic branch i ($i = LA, TA$) is defined as

$$\theta_i = \frac{\hbar\omega_{i,max}}{k_B}, \quad (2)$$

where \hbar is Planck constant, $\omega_{i,max}$ is the phonon frequency at the zone boundary of the i -th acoustic mode, and k_B is Boltzmann constant. The calculated Debye temperature θ_D

for MoS₂, MoSe₂, and WS₂ are 262.3 K, 177.6 K, and 213.6 K, respectively, which is in good agreement with previous results, *i.e.* 260-320 K for MoS₂ estimated from specific-heat measurement²⁵, 197.3±6.6 K for MoSe₂ estimated from photoconductivity measurements²⁶, 210 K for WS₂ estimated from the Lindemann formula²⁷.

Concerning thermal vibrations and the bonding forces, the Debye temperature is a measure of the temperature above which all modes begin to be excited and below which modes begin to be frozen out²⁸. We first investigate the relation between vibrational modes and the Debye temperature by calculating the projected PDOSs for the M(XY), M(Z), X(XY), and X(Z) vibrations in MX₂ structures as shown in fig. 4. Similar to the diatomic linear chain model, the scale of the acoustic (optical) phonon branch is dominated by atoms with larger (smaller) mass in three materials. As the mass ratio of all studied MX₂ (m_M/m_{2X}) in table II show, the acoustic phonon vibration in the PDOS is governed by the larger mass. The mass ratio of MoS₂ is most close to 1, while that of WS₂ is much larger 1. Therefore the low-frequency acoustic phonon branches of MoS₂ up to 233.9 cm⁻¹ are mainly from the Mo(XY), Mo(Z) and S(XY) vibrations due to similar mass, whereas those of WS₂ up to 182.3 cm⁻¹ are mainly from the W(XY) and W(Z) vibrations due to the much larger mass of W atoms. In contrast to other two materials, the mass of transition metal atoms in MoSe₂ is smaller than the mass of chalcogenide atoms. Thus, although all Mo(XY), Mo(Z), Se(XY), and Se(Z) vibrations contribute significantly to the low-frequency branches of MoSe₂ up to 157.5 cm⁻¹, the PDOS of the Se(XY) and Se(Z) vibrations is higher than other two vibrations due to the relatively larger mass of Se atoms.

Furthermore, low average atomic mass \overline{M} , besides the strong interatomic bonding mentioned above, can lead to a large Debye temperature as well. The mass differences in MoS₂, MoSe₂, and WS₂ are also shown in table II. For MoS₂ and MoSe₂ which have similar bonding characteristics as shown in fig. 3, the \overline{M} of MoS₂ is approximately two thirds the \overline{M} of MoSe₂, and the calculated θ_D is about 1.5 times larger. For WS₂, although it has close mass to MoSe₂, the strong covalent W-S bonding as shown in fig. 3, can result in relatively larger Debye temperature as implied in previous work⁹. Therefore, although the average atomic mass plays a key role in determining the Debye temperature, the effect of interatomic bonding can not be neglected and should be taken into account when studying the thermal transport properties of monolayer MX₂.

In addition, we investigate the vibrational mode of all studied MX₂. Since the monolayer

TABLE II: The mass ratio m_M/m_{2X} , average atomic mass \bar{M} , and Debye temperature θ_D of all studied MX_2 .

Structure	m_M/m_{2X}	\bar{M} (amu)	θ_D (K)
MoS ₂	1.50	53.36	262.3
MoSe ₂	0.61	84.63	177.6
WS ₂	2.87	82.66	213.6

TABLE III: Theoretical determined optical phonon frequencies (cm^{-1}) at the Γ point. The experimental results are also given in parentheses for comparison.

Structure	E''	E'	A'_1	A''_2
MoS ₂	278.4 (283 ^a)	377.2 (385 ^a)	397.7 (404 ^a)	461.6 (470 ^b)
MoSe ₂	163.3 (167 ^c)	235.7 (240 ^c)	279.3 (282 ^c)	345.2 (351 ^c)
WS ₂	291.6 (298 ^a)	350.8 (357 ^a)	413.0 (419 ^a)	432.8 (438 ^d)

^a Reference³¹

^b Reference³²

^c Reference³³

^d Reference³⁰

MX_2 belongs to the D_{3h} point group, the optical lattice-vibration modes at Γ point can be thus decomposed as

$$\Gamma_{\text{optical}} = A''_2(\text{IR}) + A'_1(\text{R}) + E'(\text{IR} + \text{R}) + E''(\text{R}), \quad (3)$$

where IR and R denote infrared- and Raman-active mode respectively. Table III lists the optical phonon frequencies at the Γ point. The calculated phonon frequencies are in agreement with the experimental results, and the discrepancy is less than 3%. The LO/TO splitting is very small and can be neglected here^{29,30}.

The schematic vibrations for the phonon modes are shown in fig. 5, where one A''_2 and one E' are acoustic modes, the other A''_2 (E') are IR (both IR and R) active as shown in Eq. (3). A''_2 and A'_1 modes vibrate along the z -direction, and E' and E'' modes vibrate in the $x - y$ direction. As shown before in fig. 4, in the case of E' (LA/TA) in monolayer MoS₂, the Mo and S atoms vibrate with similar amplitudes; for A''_2 (ZA) in MoS₂, the vibrations

of Mo atoms have much larger amplitudes. For both E' (LA/TA) and A_2'' (ZA) in monolayer MoSe₂, the Se atoms vibrate with greater amplitudes than Mo atoms. The vibration of W atoms dominates S atoms in both E' (LA/TA) and A_2'' (ZA) vibrational modes in monolayer WS₂ due to the large m_W/m_{2S} .

C. Thermodynamic properties

The Grüneisen parameter γ , which describes the thermal expansion of a crystal on its vibrational properties, provides information on the anharmonic interactions. The larger the Grüneisen parameter indicates the stronger anharmonic vibrations. The expression for the Grüneisen parameter is given by^{34,35}

$$\gamma = \frac{3\alpha BV_m}{C_V}, \quad (4)$$

where α is the linear thermal expansion coefficient, B is the bulk modulus, V_m is the molar volume, and C_V is the isometric heat capacity.

Table IV compares the calculated isometric heat capacity, bulk modulus, and linear thermal expansion coefficient with experimental results at 300 K. The isometric heat capacity can be calculated as

$$C_V = \left(\frac{\partial E}{\partial T} \right)_V = \sum_{n,\mathbf{q}} k_B \left(\frac{\hbar\omega_n(\mathbf{q})}{k_B T} \right)^2 \frac{e^{\hbar\omega_n(\mathbf{q})/k_B T}}{(e^{\hbar\omega_n(\mathbf{q})/k_B T} - 1)^2}, \quad (5)$$

where T is temperature, and $\omega_n(\mathbf{q})$ is the phonon frequency of the n -th branch with wave vector \mathbf{q} . The calculated values of C_V for MoS₂, MoSe₂, and WS₂ at room temperature are in good agreement with the experimental results^{36–38}. The bulk modulus B and linear thermal expansion coefficient α are calculated using the quasi-harmonic approximation (QHA), which takes the first-order anharmonicity into account¹⁶. The obtained B for MoS₂ is in agreement with the experimental value³⁹. For MoSe₂, the computed B is fallen in the range of measured values^{40,41}. The great discrepancies between the calculated and experimental B are seen for WS₂. Since the bulk modulus is used to describe the stiffness of MX₂¹¹, the bonding in monolayer WS₂ is found to be much stiffer comparing to other two materials. The calculated α for MoS₂ and MoSe₂ at 300 K is is fallen in the range of measured values^{33,42,43}, while larger than the measured α for WS₂.

TABLE IV: Comparison between the calculated and measured isometric heat capacity C_V (J mol⁻¹ K⁻¹), bulk modulus B (GPa), and linear thermal expansion coefficient α (10⁻⁶ K⁻¹). The experimental results are also given in parentheses.

Structure	C_V	B	α
MoS ₂	62.97 (63.55 ^a)	52.3 (53.4±1.0 ^b)	17.4 (10.7 ^c) (82 ^d)
MoSe ₂	68.75 (68.60 ^e)	57.3 (45.7±0.3 ^f) (62 ^g)	19.5 (7.24 ^h) (105 ^d)
WS ₂	63.49 (63.82±0.32 ⁱ)	77.9 (61±1 ^j)	14.8 (6.35 ^k)

^a Reference³⁶

^b Reference³⁹

^c Reference⁴²

^d Reference³³

^e Reference³⁷

^f Reference⁴⁰

^g Reference⁴¹

^h Reference⁴³

ⁱ Reference³⁸

^j Reference⁴⁴

^k Reference¹⁹

As shown in fig. 6, the temperature-dependent Grüneisen parameter is calculated using Eq. (4). The Grüneisen parameter can also be calculated by averaging the mode Grüneisen parameter $\gamma_n(\mathbf{q})$,

$$\gamma_{ave}^{mode} = \frac{1}{C_V} \sum_{n,\mathbf{q}} \gamma_n(\mathbf{q}) C_{V,n}(\mathbf{q}), \quad (6)$$

where $C_{V,n}(\mathbf{q})$ is the mode heat capacity. The mode Grüneisen parameter is given by

$$\gamma_n(\mathbf{q}) = -\frac{a_0}{\omega_n(\mathbf{q})} \frac{\partial \omega_n(\mathbf{q})}{\partial a}, \quad (7)$$

where a_0 is the equilibrium lattice constant at 0 K. Fig. 6 also shows the calculated γ_{ave}^{mode} , which is consistent with the Grüneisen parameter calculated using Eq. (4).

The frequency dependence of mode Grüneisen parameter of MoS₂ in the irreducible BZ

is plotted in fig. 7, and the mode Grüneisen parameter along symmetry directions is shown in the inset. Similar to diamond, graphite and graphene⁴⁵, negative γ_{ZA} is observed at low frequencies (under 50 cm^{-1} in MoS_2). The average Grüneisen parameter is negative at low temperatures because only the low-frequency phonons are excited, as shown in fig. 6. Our results are in agreement with previous calculations^{46,47}. The calculated γ_{ave}^{mode} at room temperature is 1.22, 1.20, and 1.15 for MoS_2 , MoSe_2 , and WS_2 , respectively, indicating that MoS_2 has the strongest bonding anharmonicity among three materials, while WS_2 has the weakest anharmonic vibrations. The bonding anharmonicity obtained from analysing the γ of all studied MX_2 is consistent with previous work¹¹.

According to Slack's expression^{8,24}, assuming that only the acoustic phonon modes participate in the heat conduction process, the lattice thermal conductivity in the temperature range where three-phonon scattering is dominant, can be given as

$$\kappa_l = A \frac{\overline{M} \theta_D^3 \delta n^{1/3}}{\gamma^2 T}, \quad (8)$$

where \overline{M} is the average mass of an atom in the crystal, δ^3 is the volume per atom, n is the number of atoms in the primitive unit cell, and A is a constant which is given by⁴⁸

$$A = \frac{2.43 \times 10^{-6}}{1 - 0.514/\gamma + 0.228/\gamma^2} \quad (9)$$

when the units of κ_l , \overline{M} , and δ are taken as W/mK, amu, and Å, respectively. The obtained lattice thermal conductivity for monolayer MoS_2 , MoSe_2 , and WS_2 at room temperature is 33.6 W/mK, 17.6 W/mK, and 31.8 W/mK, respectively, which is in good agreement with the experimental value of 34.5 ± 4 W/mK for monolayer MoS_2 ⁶, and 32 W/mK for monolayer WS_2 ⁷. Although there is no experimental value for monolayer MoSe_2 , our calculated κ_l is a reasonable prediction.

The Slack's expression attempts to normalize the effect of mass density, crystal structure, interatomic bonding, and anharmonicity⁸⁻¹⁰. MoS_2 , MoSe_2 , and WS_2 have similar crystal structure. The factor $\overline{M} \theta_D^3 \delta$ in Eq. (8) is maximized for light mass, strong bonded crystals, because low average atomic mass and strong interatomic bonding lead to a high θ_D^3 , and the θ_D^3 term dominates the behaviour⁸. The Debye temperature reflects the magnitude of sound velocity. Higher Debye temperature results in increased phonon velocities, and increased acoustic-phonon frequencies as mentioned above, which suppress phonon-phonon scattering

by decreasing phonon populations. Therefore the high thermal conductivity of MoS₂ is related to its high Debye temperature, which is due to its much lower average atomic mass.

Recent theoretical work has predicted that monolayer WS₂ has the highest thermal conductivity among all studied MX₂ at room temperature due to a large frequency gap between its acoustic and optic phonons⁵, which originates in its larger mass ratio m_W/m_{2S} . Our results suggest that the average atomic mass plays a key role in determining the phonon dispersion of MoS₂ and WS₂, and subsequently determines the Debye temperature from which the phonon velocities can be estimated. In addition, although WS₂ has similar average atomic mass to MoSe₂, its strong W-S bonding leads to a higher Debye temperature. Furthermore, small γ of WS₂ means low anharmonicity, which also results in a higher thermal conductivity. Therefore the thermal conductivity of WS₂ is determined by the competition between high average atomic mass, strong covalent W-S bonding and low anharmonicity.

IV. CONCLUSION

In summary, we investigate the lattice dynamics and thermodynamic properties of MoS₂, MoSe₂, and WS₂ by first principles calculations. The obtained phonon frequencies and lattice thermal conductivity agree well with experimental measurements. Our calculations show that the thermal conductivity of MoS₂ is highest among the three materials due to its large Debye temperature, which is attributed to the lowest average atomic mass. We also find that WS₂ has stronger covalent W-S bonding and lower anharmonicity, leading to much higher thermal conductivity compared to MoSe₂.

Acknowledgement

This work is supported by the National Natural Science Foundation of China under Grants No. 11374063 and 11404348.

References

- ¹ B. F. Ferrari Andrea C and et. al., *Nanoscale* **7**, 4598 (2015).
- ² J. Klinovaja and D. Loss, *Phys. Rev. B* **88**, 075404 (2013).
- ³ M. Buscema, M. Barkelid, V. Zwiller, H. S. J. van der Zant, G. A. Steele, and A. Castellanos-Gomez, *Nano Letters* **13**, 358 (2013).
- ⁴ J. M. Ziman, *Electrons and Phonons: The Theory of Transport Phenomena in Solids* (Oxford University Press, 1960).
- ⁵ X. Gu and R. Yang, *Applied Physics Letters* **105**, 131903 (2014).
- ⁶ R. Yan, J. R. Simpson, S. Bertolazzi, J. Brivio, M. Watson, X. Wu, A. Kis, T. Luo, A. R. Hight Walker, and H. G. Xing, *ACS Nano* **8**, 986 (2014).
- ⁷ N. Peimyoo, J. Shang, W. Yang, Y. Wang, C. Cong, and T. Yu, *Nano Research* **8**, 1210 (2015).
- ⁸ G. A. Slack, *Journal of Physics and Chemistry of Solids* **34**, 321 (1973).
- ⁹ L. Lindsay, D. A. Broido, and T. L. Reinecke, *Phys. Rev. Lett.* **111**, 025901 (2013).
- ¹⁰ A. Jain and A. J. McGaughey, *Journal of Applied Physics* **116**, 073503 (2014).
- ¹¹ L.-F. Huang and Z. Zeng, *The Journal of Physical Chemistry C* **119**, 18779 (2015).
- ¹² Y. Gong, Z. Liu, A. R. Lupini, G. Shi, J. Lin, S. Najmaei, Z. Lin, A. L. Elias, A. Berkdemir, G. You, et al., *Nano Letters* **14**, 442 (2014).
- ¹³ D. O. Dumcenco, H. Kobayashi, Z. Liu, Y.-S. Huang, and K. Suenaga, *Nat Commun* **4**, 1351 (2013).
- ¹⁴ G. Kresse and J. Furthmüller, *Phys. Rev. B* **54**, 11169 (1996).
- ¹⁵ S. Baroni, S. de Gironcoli, A. Dal Corso, and P. Giannozzi, *Rev. Mod. Phys.* **73**, 515 (2001).
- ¹⁶ A. Togo, F. Oba, and I. Tanaka, *Phys. Rev. B* **78**, 134106 (2008).
- ¹⁷ A. Molina-Sánchez and L. Wirtz, *Phys. Rev. B* **84**, 155413 (2011).
- ¹⁸ R. Coehoorn, C. Haas, J. Dijkstra, C. J. F. Flipse, R. A. de Groot, and A. Wold, *Phys. Rev. B* **35**, 6195 (1987).
- ¹⁹ A. Matthäus, A. Ennaoui, S. Fiechter, S. Tiefenbacher, T. Kiesewetter, K. Diesner, I. Sieber, W. Jaegermann, T. Tsirlina, and R. Tenne, *Journal of The Electrochemical Society* **144**, 1013 (1997).

- ²⁰ K. F. Mak, C. Lee, J. Hone, J. Shan, and T. F. Heinz, *Phys. Rev. Lett.* **105**, 136805 (2010).
- ²¹ P. Tonndorf, R. Schmidt, P. Böttger, X. Zhang, J. Börner, A. Liebig, M. Albrecht, C. Kloc, O. Gordan, D. R. T. Zahn, et al., *Opt. Express* **21**, 4908 (2013).
- ²² H. R. Gutiérrez, N. Perea-López, A. L. Elías, A. Berkdemir, B. Wang, R. Lv, F. López-Urías, V. H. Crespi, H. Terrones, and M. Terrones, *Nano Letters* **13**, 3447 (2013).
- ²³ A. Kumar and P. Ahluwalia, *The European Physical Journal B* **85**, 186 (2012), ISSN 1434-6028.
- ²⁴ D. T. Morelli and J. P. Heremans, *Applied Physics Letters* **81**, 5126 (2002).
- ²⁵ Y. S. Touloukian and E. H. Buyco, eds., *Specific Heat-Nonmetallic Solids, in Thermal Properties of Matter: The TPRC Data Series*, vol. 5 (New York: IFI/Plenum, 1970).
- ²⁶ S. Hu, Y. Lee, J. Shen, K. Chen, K. Tiong, and Y. Huang, *Solid State Communications* **139**, 176 (2006).
- ²⁷ C. H. Ho, C. S. Wu, Y. S. Huang, P. C. Liao, and K. K. Tiong, *Journal of Physics: Condensed Matter* **10**, 9317 (1998).
- ²⁸ T. Nakashima and Y. Umakoshi, *Philosophical Magazine Letters* **66**, 317 (1992).
- ²⁹ Y. Cai, J. Lan, G. Zhang, and Y.-W. Zhang, *Phys. Rev. B* **89**, 035438 (2014).
- ³⁰ R. D. Luttrell, S. Brown, J. Cao, J. L. Musfeldt, R. Rosentsveig, and R. Tenne, *Phys. Rev. B* **73**, 035410 (2006).
- ³¹ X. Zhang, X.-F. Qiao, W. Shi, J.-B. Wu, D.-S. Jiang, and P.-H. Tan, *Chem. Soc. Rev.* **44**, 2757 (2015).
- ³² T. J. Wieting and J. L. Verble, *Phys. Rev. B* **3**, 4286 (1971).
- ³³ D. J. Late, S. N. Shirodkar, U. V. Waghmare, V. P. Dravid, and C. N. R. Rao, *Chem. Phys. Chem.* **15**, 1592 (2014).
- ³⁴ G. Grimvall, *Thermophysical properties of materials* (Amsterdam: Elsevier, 1999).
- ³⁵ H. Shao, X. Tan, T. Hu, G.-Q. Liu, J. Jiang, and H. Jiang, *EPL (Europhysics Letters)* **109**, 47004 (2015).
- ³⁶ L. S. Volovik, V. V. Fesenko, A. S. Bolgar, S. V. Drozdova, L. A. Klochkov, and V. F. Primachenko, *Soviet Powder Metallurgy and Metal Ceramics* **17**, 697 (1978).
- ³⁷ A. S. Blinder, A. V. Bolgar and Z. A. Trofimova, *Powder Metallurgy and Metal Ceramics* **32**, 234 (1993).
- ³⁸ P. A. G. O'hare, W. Hubbard, G. Johnson, and H. Flotow, *The Journal of Chemical Thermodynamics* **16**, 45 (1984).

- ³⁹ R. Aksoy, Y. Ma, E. Selvi, M. Chyu, A. Ertas, and A. White, *Journal of Physics and Chemistry of Solids* **67**, 1914 (2006).
- ⁴⁰ R. Aksoy, E. Selvi, and Y. Ma, *Journal of Physics and Chemistry of Solids* **69**, 2138 (2008).
- ⁴¹ Z. Zhao, H. Zhang, H. Yuan, S. Wang, Y. Lin, Q. Zeng, G. Xu, Z. Liu, G. K. Solanki, K. D. Patel, et al., *Nat Commun* **6**, 7312 (2015).
- ⁴² E. M. Dudnik and O. V. Kh., *Soviet Powder Metallurgy and Metal Ceramics* **5**, 125 (1966).
- ⁴³ S. H. El-Mahalawy and B. L. Evans, *J. Appl. Crystallogr.* **9**, 403 (1976).
- ⁴⁴ E. Selvi, Y. Z. Ma, R. Aksoy, A. Ertas, and A. White, *Journal of Physics and Chemistry of Solids* **67**, 2183 (2006).
- ⁴⁵ N. Mounet and N. Marzari, *Phys. Rev. B* **71**, 205214 (2005).
- ⁴⁶ L. F. Huang, P. L. Gong, and Z. Zeng, *Phys. Rev. B* **90**, 045409 (2014).
- ⁴⁷ C. Sevik, *Phys. Rev. B* **89**, 035422 (2014).
- ⁴⁸ C. L. Julian, *Phys. Rev.* **137**, A128 (1965).

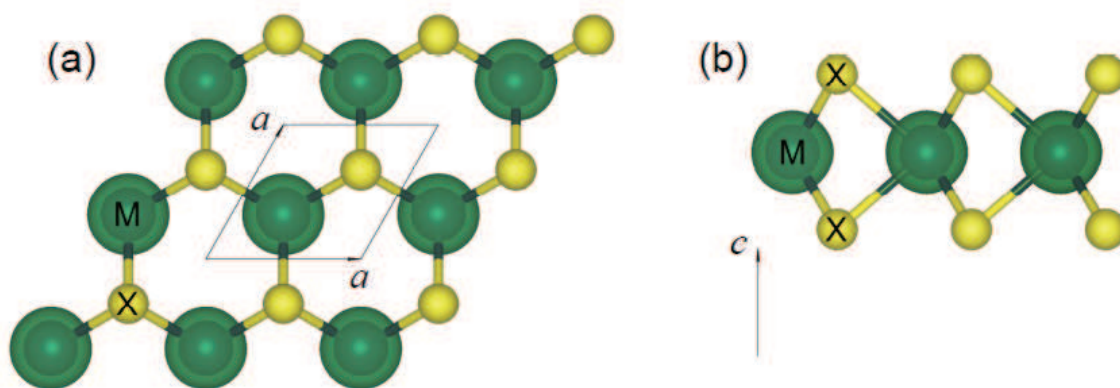


FIG. 1: (a) Top view and (b) side view of crystal structure of monolayer MX_2 . The primitive vectors are $\mathbf{a}(a,0,0)$, $\mathbf{b}(a/2,\sqrt{3}a/2,0)$, and $\mathbf{c}(0,0,c)$.

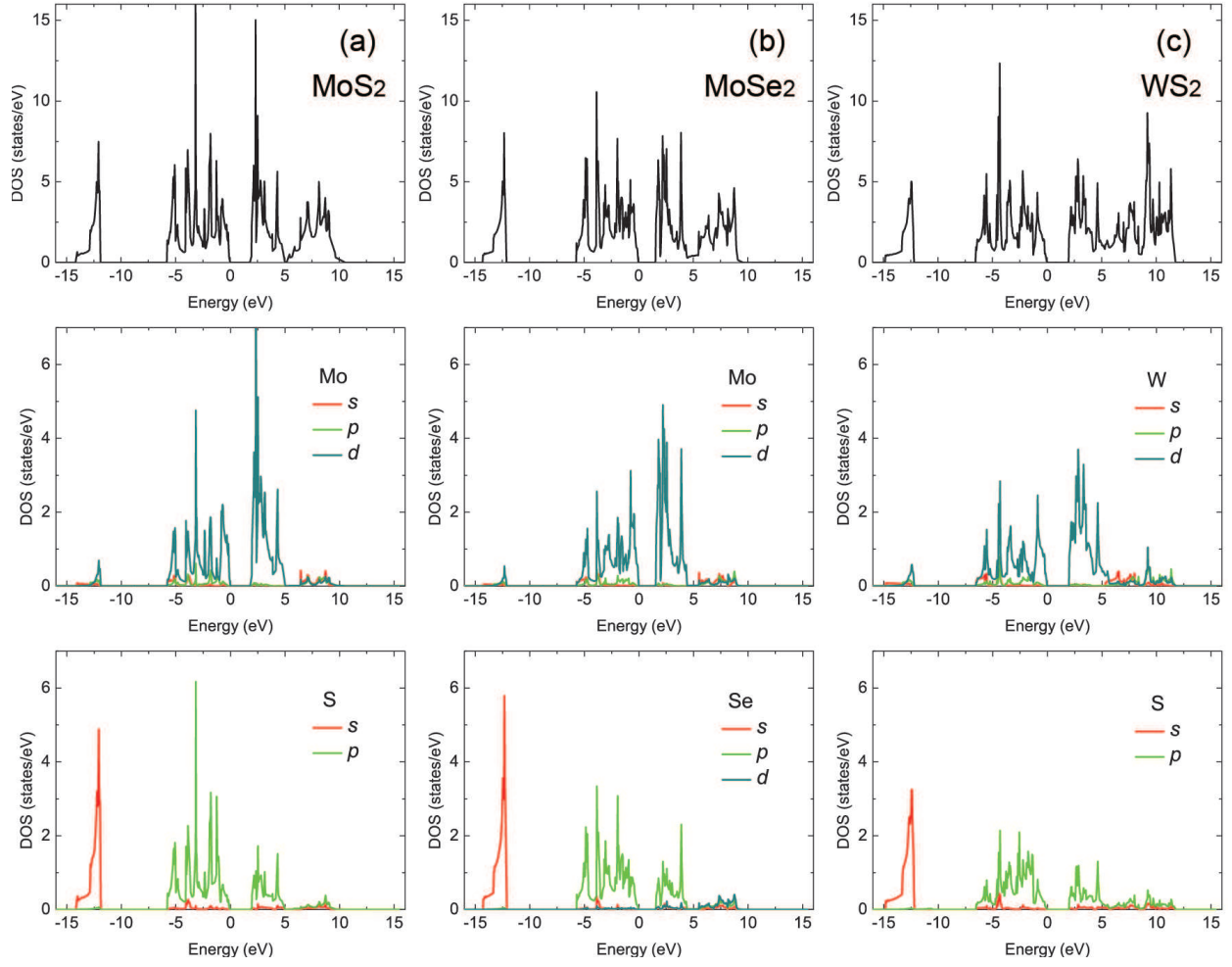


FIG. 2: Total and atom projected DOS for (a)MoS₂, (b)MoSe₂, and (c)WS₂.

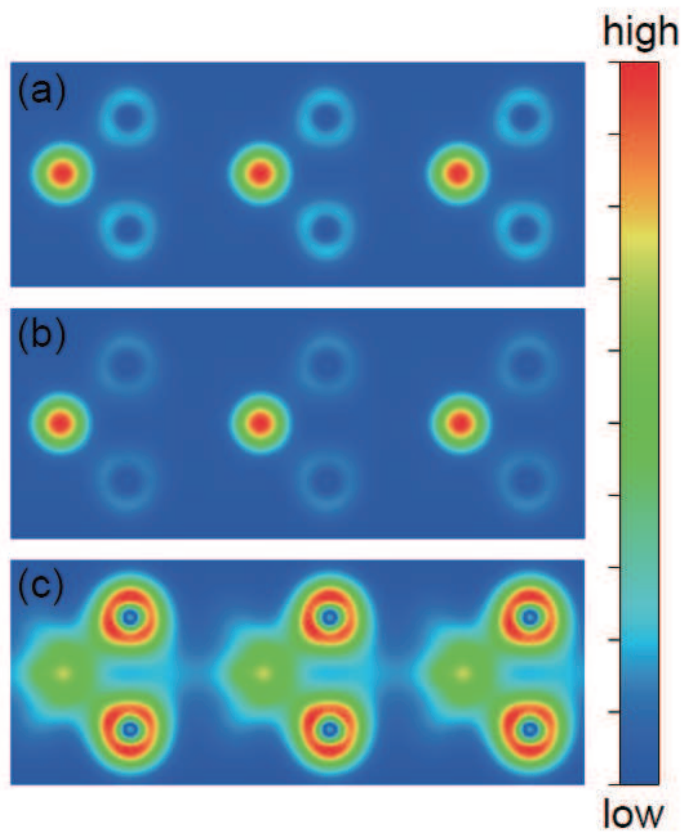


FIG. 3: Electronic charge density of (a) MoS_2 , (b) MoSe_2 , and (c) WS_2 in the $[1\bar{1}0]$ plane.

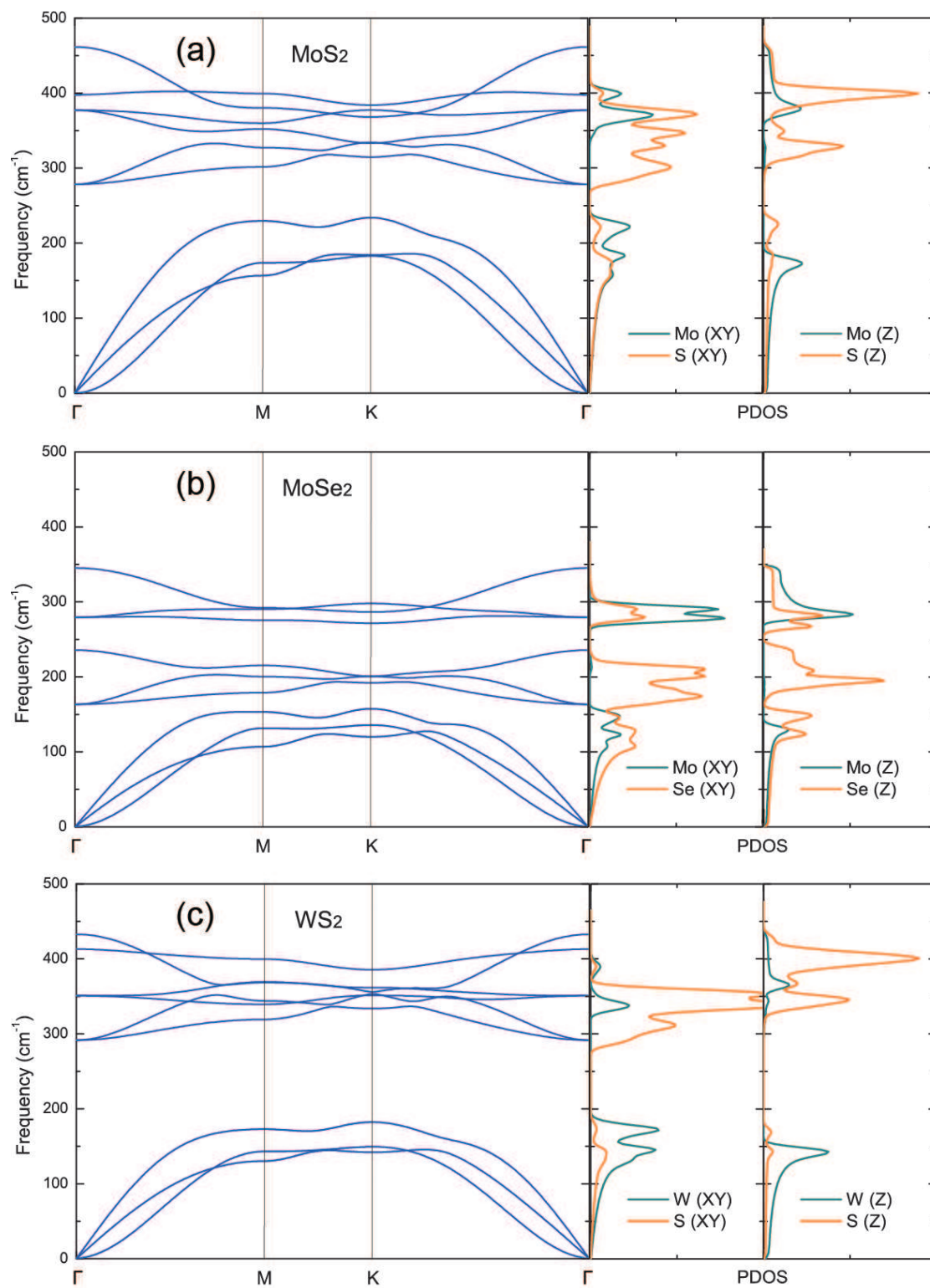


FIG. 4: Phonon spectra and projected PDOS for (a)MoS₂, (b)MoSe₂, and (c)WS₂.

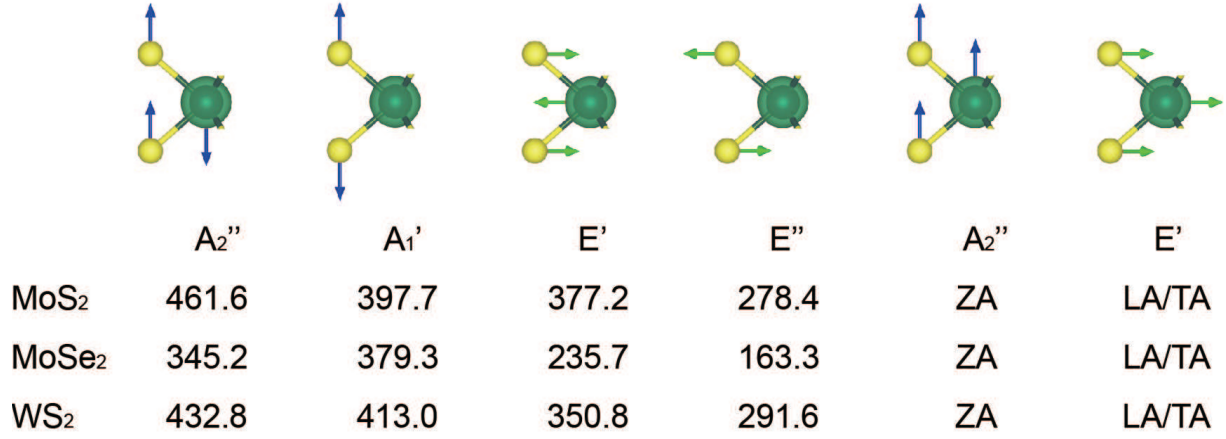


FIG. 5: Schematic phonon vibrations with different frequencies (cm^{-1}).

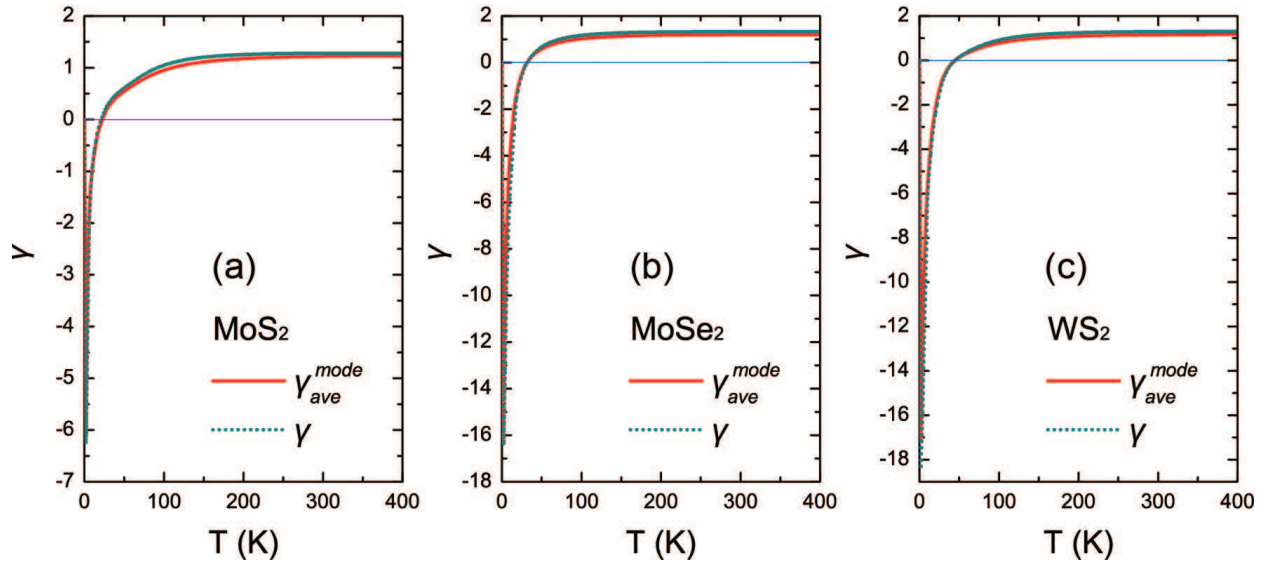


FIG. 6: Calculated temperature-dependent Grüneisen parameter for (a)MoS₂, (b)MoSe₂, and (c)WS₂.

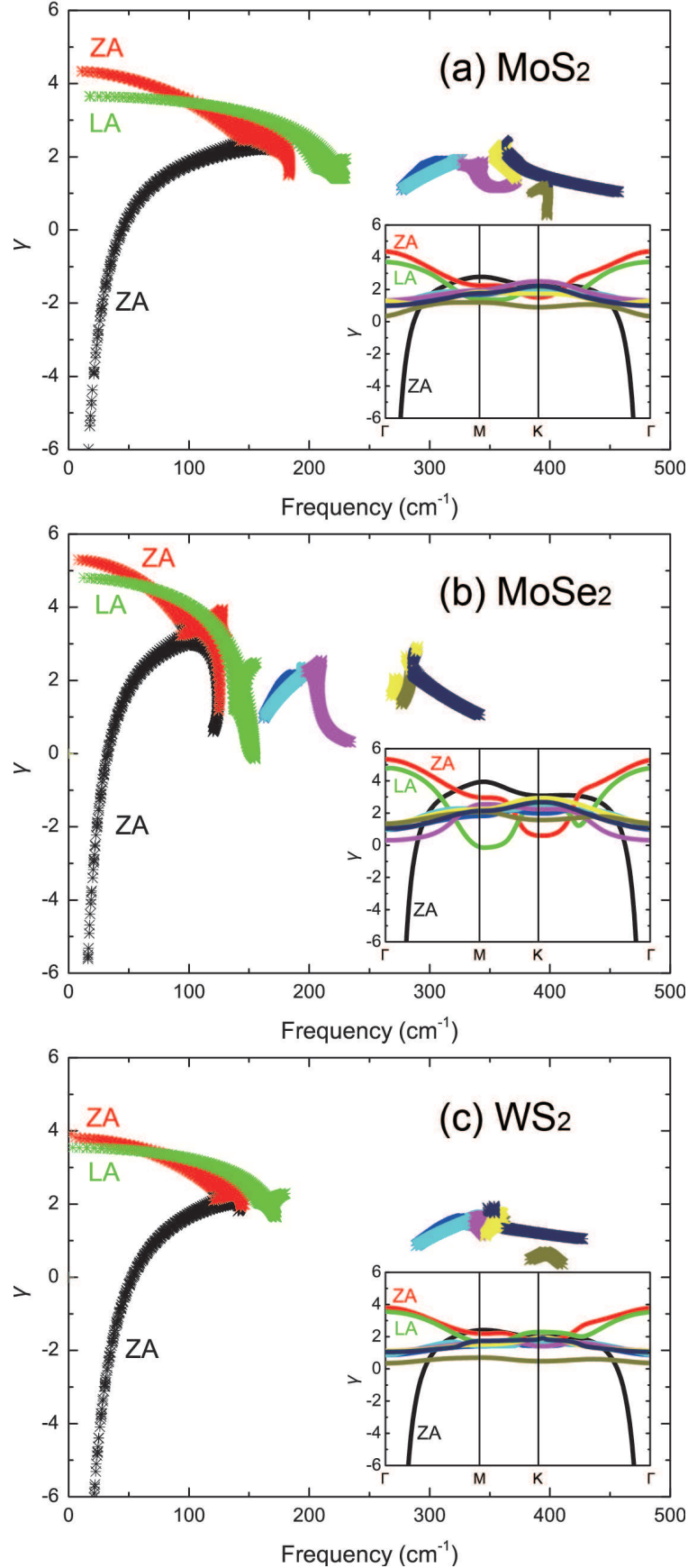


FIG. 7: Calculated mode Grüneisen parameter for (a)MoS₂, (b)MoSe₂ and (c)WS₂ with respect to frequencies, and with respect to wave vectors as shown in the inset.